Additive Manufacturing: Metallurgy, Cut Analysis & Porosity

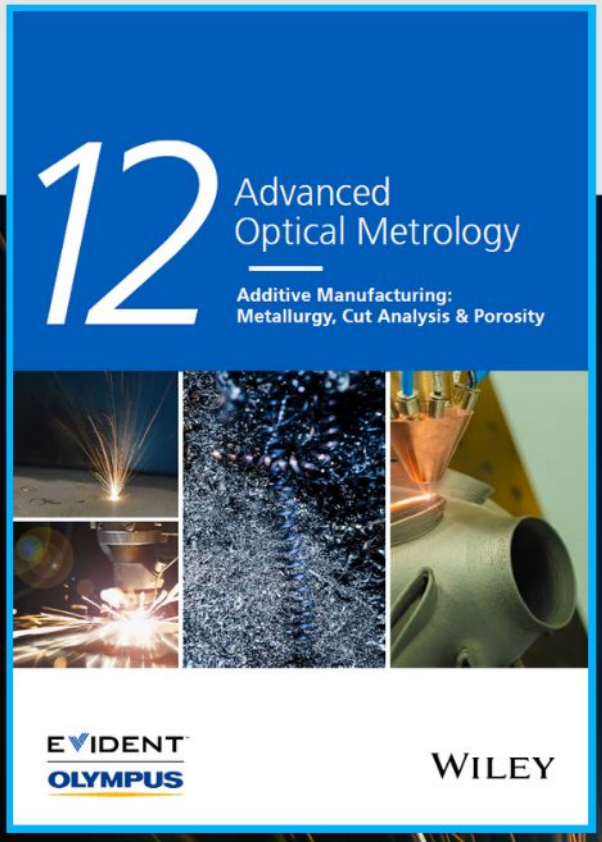

The latest eBook from Advanced Optical Metrology. Download for free.

In industry, sector after sector is moving away from conventional production methods to additive manufacturing, a technology that has been recommended for substantial research investment.

Download the latest eBook to read about the applications, trends, opportunities, and challenges around this process, and how it has been adapted to different industrial sectors.

EVIDENT
OLYMPUS

WILEY

ADVANCED FUNCTIONAL MATERIALS
www.afm-journal.de

Precise Control of Li^+ Directed Transport via Electronegative Polymer Brushes on Polyolefin Separators for Dendrite-Free Lithium Deposition

Shujun Zheng, Lulu Mo, Kai Chen, Ai-Long Chen, Xu Zhang, Xiaoshan Fan, Feili Lai, Qingcong Wei, Yue-E Miao, Tianxi Liu,* and Yan Yu**

Nonuniform ion flux triggers uneven lithium (Li) deposition and continuous dendrite growth, severely restricting the lifetime of Li-metal batteries (LMBs). Herein, an electronegative poly(pentafluorophenyl acrylate) (PPFPA) polymer brush-grafted Celgard separator signed as PPFPA-g-Celgard is designed to precisely construct one-dimensionally directed Li^+ flux at the nanoscale so as to realize faster ion transport and ultra-stable Li deposition. The grafting of PPFPA polymer chains is enabled by the simple bio-inspired engineering of surface-initiated atom transfer radical polymerization chemistry. Both theoretical and experimental analyses demonstrate an obvious increase by almost two times in Li^+ affinity and ion transfer kinetics for PPFPA-g-Celgard over the Celgard separator. Reversible and stable Li plating/stripping can be realized by rapidly switching from 0.5 to 6 mA cm^{-2}. Besides, the Li | PPFPA-g-Celgard | $LiFePO_4$ full cell exhibits universal and long-term cyclability with a capacity retention of 83% over 700 cycles in ether electrolyte and 92.9% for over 300 cycles in carbonate electrolyte as well. This study represents a new direction for the general design of advanced separators with typical surface topochemistry and self-limited ion transport channels in the application of high-performance LMBs.

1. Introduction

With the highest theoretical capacity (3860 mA h g^{-1}) and lowest electrode potential (−3.04 V), lithium (Li) metal has been considered as a promising anode for high-energy-density rechargeable Li-metal batteries (LMBs).[1–5] However, nonuniform ion flux during the plating/stripping process will easily lead to the uneven distribution and concentration of Li-ions (Li^+) at the anode/electrolyte interface, bringing about Li agglomeration at "hot spots" and dendrite formation.[6–8] Meanwhile, the transport and plating rate discrepancy of Li^+ in the electrolyte and at the anode surface inevitably results in the huge polarization of ion concentration and aggravates the propagation of dendrite (**Figure 1**a).[9–11] In this regard, regulating ion transport to simultaneously achieve homogeneous ion concentration and reduced concentration polarization plays a critical role in Li deposition behaviors.

S. Zheng, L. Mo, K. Chen, A.-L. Chen, X. Zhang, X. Fan, Y.-E. Miao, T. Liu
State Key Laboratory for Modification of Chemical Fibers and Polymer Materials
College of Materials Science and Engineering
Donghua University
Shanghai 201620, China
E-mail: yuee_miao@dhu.edu.cn; txliu@dhu.edu.cn

F. Lai
Department of Chemistry
KU Leuven
Celestijnenlaan 200F, Leuven 3001, Belgium

Q. Wei
Manufacturing of Fine Chemicals
Key Laboratory of Green Chemical Media and Reactions
Ministry of Education
Henan Engineering Laboratory of Chemical Pharmaceutical and Biomedical Materials
School of Chemistry and Chemical Engineering
Henan Normal University
Xinxiang, Henan 453007, China

T. Liu
Key Laboratory of Synthetic and Biological Colloids
Ministry of Education
School of Chemical and Material Engineering
Jiangnan University
Wuxi 214122, China

Y. Yu
Hefei National Research Center for Physical Sciences at the Microscale
Department of Materials Science and Engineering
National Synchrotron Radiation Laboratory
CAS Key Laboratory of Materials for Energy Conversion
University of Science and Technology of China
Hefei, Anhui 230026, China
E-mail: yanyumse@ustc.edu.cn

The ORCID identification number(s) for the author(s) of this article can be found under https://doi.org/10.1002/adfm.202201430.

DOI: 10.1002/adfm.202201430

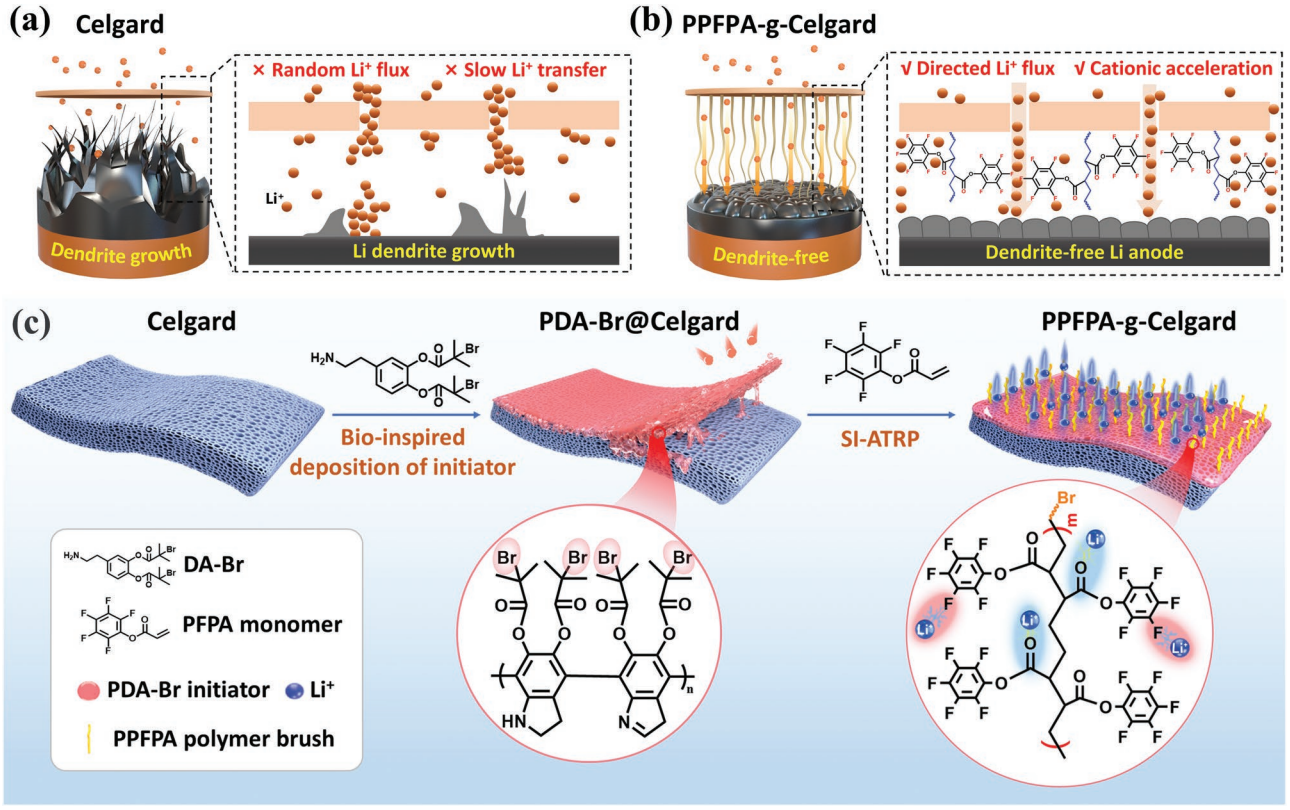

Figure 1. a,b) Schematic illustration of the structural evolution of lithium metal deposition in LMBs with different separators. c) Schematic illustration showing the chemical synthesis process of the electronegative PPFPA polymer brushes on the Celgard separator.

Currently, researchers have employed a variety of strategies to regulate uniform Li deposition, including using functionalized hosts,[7,12] effective electrolyte engineering,[13,14] and interlayer modifications.[15–17] It is known that well-designed conductive hosts with a large specific surface area can regulate ion distribution by reducing local current density.[7,18] Moreover, the lithophilic chemistry of polar groups such as C=N, −C−O, and −O−H in the matrix could accelerate cation transport,[19–21] but the unstable structure may cause drastic capacity decay. In addition, high-concentration salt electrolyte and fluorinated solvents have also been adopted to modify the physicochemical properties of solid electrolyte interface (SEI) films.[22] For instance, increasing the concentration of salts could endow high current density and improve the transference number of cations, thus expediting ion diffusion and prolonging the nucleation time of dendrites.[9] However, the mechanism and composition of electrolyte-derived SEI remain controversial and is not very controllable, respectively.[23] In order to facilely achieve tunable structure and composition, the interfacial engineering of both artificial SEI layers and separators at the anode/electrolyte interface, including conductive alloy layers,[6,24] lithophilic-rich organic components,[25] and their hybrids,[26,27] have been applied to stabilize the Li anode by redistributing Li^+ flux and providing fast ion diffusion. For example, Lu et al. developed a dihydroxyviolanthron (DHV) layer by taking an in situ formation approach.[28] Tang et al. designed a diamond-like carbon (DLC) coating layer to homogenize Li deposition via the in situ chemical lithiation method.[29] However, it is almost impossible to achieve the uniformity of ion flux and lower concentration polarization at the nanometer scale, and these designs are yet unable to regulate Li^+ transport paths with specially aligned ion diffusion behaviors. Furthermore, thicker organic coating interlayers inevitably impedes ion diffusion at the expense of ionic conductivity and electrochemical performance at high rates. Hence, stable LMBs are in urgent need of an ultrathin interfacial layer with Li^+ directed transport nanochannels and high ion conductivity.

Typically as polymer chains anchored on the substrate surface, polymer brushes are synthesized by a general atom transfer radical polymerization (ATRP) method.[30,31] Unique surface topochemistry enables the precise and versatile grafting of high-density polymer brushes on the modified substrate at the nanometer scale,[32] which is supposed to induce directed ion transport channels along (1D) polymer chains. Herein, an electronegative poly(pentafluorophenyl acrylate) (PPFPA) polymer brush-grafted Celgard separator, denoted as PPFPA-g-Celgard, was proposed by a polydopamine (PDA)-assisted surface initiated ATRP (SI-ATRP) strategy for the first time to precisely induce highly aligned ion transport nanochannels for stable and dendrite-free Li electrodeposition in LMBs (Figure 1b). The most electronegative sites between F and O atoms on the surface of polar PPFPA polymer chains can be effective in improving the electrolyte wettability and lithiophilicity of the Celgard separator. In particular, it is favorable for achieving rapid Li^+ diffusion and a lower ion concentration gradient, thus suppressing Li dendrite growth.

Different from traditional physically-coated separators,[33–35] the self-adhesive prime of PDA guarantees the strong interfacial coupling between PPFPA polymer brushes and the Celgard substrate. Besides, ion transport behaviors through the Celgard separator can be well maintained in that the bio-inspired self-polymerization of dopamine (DA) containing 2-bromoisobutyryl bromide (DA-Br) initiator can fully duplicate the initial porous structure of the Celgard substrate. Calculation assisted by characterization tracks that the PPFPA-g-Celgard separator could significantly improve Li^+ transfer kinetics by strong Li^+ affinity from the electronegative sites on PPFPA chains. In addition, highly directed 1D Li^+ flux paths created by uniform PPFPA polymer brushes can induce the uniform nucleation and deposition of Li metal in both ether and carbonate electrolytes. Thus, the symmetric cell with a PPFPA-g-Celgard separator achieves stable Li plating/stripping at a variation rate of 0.5 to 6 mA cm^{-2}. For practical demonstration, the assembled Li | PPFPA-g-Celgard | $LiFePO_4$ full cell can achieve a high specific capacity of 150.2 mA h g^{-1} with a capacity retention of 83% for >700 cycles. The PDA-assisted SI-ATRP strategy of rationally fabricating functional separators with highly tunable surface topochemistry holds great potential for developing high-energy and long-life LMBs.

2. Results and Discussion

Concretely, the fabrication process of the PPFPA-g-Celgard separator comprises an initial self-polymerization of the initiator-embedded dopamine monomer and subsequent SI-ATRP process, as illustrated in Figure 1c and Figure S1 (Supporting Information).[36] First, the di-*tert* butyl decarbonate (Boc_2O) agent was introduced to protect the amino group of DA, which produces the DA-Boc monomer. Then, the initiator of α-bromoisobutyryl bromide (BIBB) was embedded by connecting to the hydroxyl groups of DA-Boc monomer, which was followed by the deprotection of amino groups to obtain the final product of DA-Br (Figure S1, Supporting Information). The characteristic signals corresponding to the $-CH_3$ (31.8 ppm), tertiary carbon (56.6 ppm) and −C=O−O (171.8 ppm) groups of BIBB are detected in the ^{13}C NMR of DA-Br monomer (Figure S2, Supporting Information). Subsequently, the self-polymerization of DA-Br in the Tris solution at 30 °C could generate the uniform coating layer of initiator-embedded polydopamine (PDA-Br) on the surface of the Celgard separator.[37,38] The thickness of the macroinitiator layer can be controlled by adjusting the self-polymerization time of DA-Br in the solution (Figure S3, Supporting Information). The ionic conductivity of PDA-Br@Celgard decreases with the increasing thickness of the PDA-Br coating layer, indicating that the proper imbedding time of the macroinitiator is ≈3 h (Figure S4 and Table S1, Supporting Information). As indicated by elemental mappings (Figure S5, Supporting Information), rich C, N, O, and Br elements are homogeneously distributed on the Celgard surface, confirming the strong immobilization of the PDA-Br layer. Afterward, the terminal Br atom on Celgard acted as the initial grafting point to induce SI-ATRP reaction and achieve high-density PPFPA polymer brushes.[39] The scan electron microscope (SEM) image of PPFPA-g-Celgard with uniform elemental distributions (**Figure 2**a) shows almost no morphological change compared with those of Celgard and PDA-Br@Celgard separators (Figure S6, Supporting Information). It was also reflected by the 3D surface topography in atomic force microscope (AFM) images (Figure 2b), with a slighter change in surface roughness in comparison with the Celgard separator (Figure S7, Supporting Information). The intuitive capillary flow aperture analyzer (CFP) results indicate a mean pore size of 26 nm for the PPFPA-g-Celgard separator (Figure S8, Supporting Information), further demonstrating that the PDA-assisted SI-ATRP strategy can not only achieve highly controllable polymer brushes but also maintain the original porous structure of the Celgard separator.

To verify the successful immobilization of PPFPA polymer brushes, Fourier transform infrared (FTIR) and X-ray photoelectron spectroscopy (XPS) spectra were collected at different reaction stages. In the FTIR spectra of Figure 2c, peaks at 1454 and 1375 cm^{-1} are ascribed to the stretching vibration of $-CH_2$ in the Celgard substrate.[38] After the self-polymerization of DA-Br, the intensity of $-CH_2$ arising from the Celgard separator is reduced, whereas a strong adsorption peak appears at 1662 cm^{-1}, corresponding to the benzene rings in PDA-Br.[40,41] This indicates the successful adhesion of PDA-Br layer on the Celgard substrate, which is in good agreement with the energy dispersive spectrometer (EDS) results (Figure S5, Supporting Information). Upon polymerization, the C=C stretching vibration in the PFPA monomer at ≈1620 cm^{-1} disappears, and the PPFPA-g-Celgard separator shows an obvious peak at 1730 cm^{-1}, which is assigned to the carbonyl bond (−C=O) in PPFPA polymer chains.[42,43] The disappeared typical peaks at 185.02 eV (Br 3p) and 71.76 eV (Br 3d), as well as the presence of 686.88 eV (F 1 s) in XPS survey spectra, also certify the achievement in grafting with PPFPA polymer brushes (Figure 2d). To probe into the composition distribution of PPFPA polymer brushes on the Celgard surface, a high-resolution XPS depth-profile analysis was performed at an Ar-ion etching speed of 1.5 nm min^{-1}. As shown in Figure 2e, the F atom is concentrated at the first four etching stages but decreases dramatically with the increase of sputtering time. Additionally, a new peak ascribed to the Br atom from the remaining PDA-Br layer emerges. Based on the atomic change of XPS data, the thickness of PPFPA polymer brushes is calculated to be ≈6 nm, further confirming the broad selectivity of monomers and controllable technical advantages of the PDA-assisted SI-ATRP strategy.

The ion transport behavior of the PPFPA-g-Celgard separator in the electrolyte is a critical indicator. The electrostatic potential (ESP) calculations indicate that negative charge is strongly concentrated on the O and F sites in PPFPA compared with that on the isopotential surface of Celgard (Figure 2f), which can induce rapid Li^+ transport within the highly-directed 1D ion flux channels formed by PPFPA. Density functional theory (DFT) calculations were conducted to further evaluate coordination ability toward Li^+. Three configurations of adsorption sites were considered for the PPFPA-g-Celgard separator with the adsorption energy of –2.26, –1.53, and –1.47 eV, respectively, outperforming the value of –0.04 eV for the bare Celgard separator (Figure 2g; Figure S9, Supporting Information). This verifies that a lithophilic environment is generated with the chemical grafting of the PPFPA layer, which indeed would

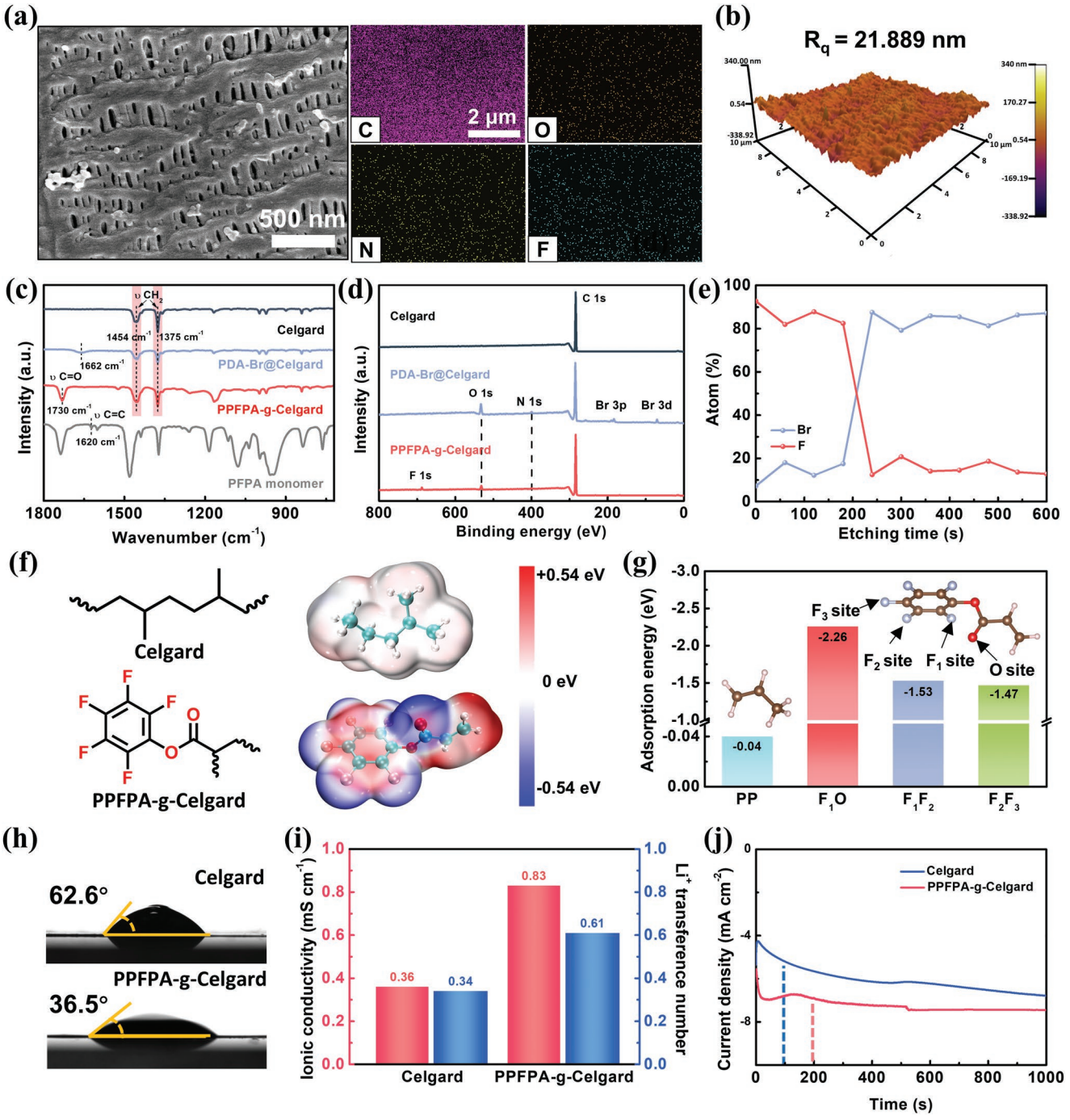

Figure 2. a) The SEM image and corresponding EDS mapping and b) AFM image and the corresponding roughness of PPFPA-g-Celgard separator. c) FTIR and d) XPS spectra of different samples. e) The composite distribution of Br and F elements in PPFPA-g-Celgard through Ar^+ etching detection in XPS. f) The calculated ESP, and g) Different adsorption sites and the corresponding adsorption energy of Li atom on Celgard and PPFPA-g-Celgard separators. h) The static contact angles of the electrolyte on Celgard and PPFPA-g-Celgard separators. i) The ionic conductivity and Li^+ transference number, and j) Chronoamperograms of different separators at an overpotential of −150 mV.

reduce the ion concentration gradient and prohibit the growth of Li dendrite by effectively redistributing Li^+ flux during discharge/charge. Benefitting from the strong affinity between electronegative PPFPA polymer brushes and Li^+, the PPFPA-g-Celgard separator exhibit enhanced wettability toward the polar electrolyte with a decreased contact angle of 36.5° (Figure 2h) and increased electrolyte uptake (209%) and retention (48%; Figure S10, Supporting Information). In contrast, the electrolyte contact angle of Celgard is as high as 62.6°, along with relatively low electrolyte uptake (108%) and retention (20%) due to the poor electrolyte wettability of Celgard. Therefore, the PPFPA-g-Celgard separator presents a higher ion conductivity

of 8.33×10^{-4} S cm^{-1} compared with Celgard (3.6×10^{-4} S cm^{-1}) in conventional Li | Li symmetrical cells (Figure 2i; Figure S11, Supporting Information). Additionally, it shows an extremely high Li^+ transference number of 0.61 compared with the unmodified Celgard of only 0.34 (Figure 2i; Figure S12, Supporting Information). This enhancement may be ascribed to the electronegative functional groups in the PPFPA-g-Celgard separator, which would impede the migration of $TFSI^-$ anions and promote the transference of cations.[44] The dynamic difference of Li–ion diffusion was also verified by the chronoamperograms (CA) test at a potential of –150 mV (Figure 2j). For the Celgard separator, its current density keeps fluctuating over 200 s, indicating a long and chaotic Li–ion diffusion process along with the random surface nucleation of Li metal. On the contrary, the Li–ion diffusion based on the PPFPA-g-Celgard separator lasts <100 s, suggesting that the long-range disordered Li^+ diffusion is redistributed and replaced by the short-range order paths of the 1D directional polymer-brush structure. Besides, the enhanced ionic conductivity and transference number of cations also helped to suppress dendrites according to the space-charge theory.[45] As a result, adjustable, uniform and firmly attached PDA-assisted PPFPA polymer brushes can effectively optimize ionic diffusion kinetics and redistribute ion-flux, thereby achieving uniform Li deposition.

To evaluate the deposition evolution of Li metal with PPFPA polymer brushes, dissipative particle dynamics (DPD) simulation was performed,[46] in that the brown balls on the anode surface were assumed to stand for Li metal deposition. The number of Li^+ was set as 4000 to control the ion concentration gradient. For the PPFPA-g-Celgard separator, orderly arranged high-density curves were introduced to mimic electronegative polymer brushes (**Figure 3**a; Figure S13 and Table S2, Supporting Information). After releasing initial constraints, Li^+ would rapidly go through the Celgard separator and an obvious bump appears at a short diffusion time (t = 110 τ), as shown in Figure 3b. In the subsequent deposition process (t = 220, 330 τ), apparent Li accumulation on the "hotspot" surface would rapidly evolve into dendrites, eventually, puncture the separator and induce thermal runaway. In sharp contrast, uniform Li deposition without dendritic morphology is observed in the PPFPA simulation box even after a prolonged simulation time, as displayed in the real-time evolution process (Figure 3c). The different deposition behavior can result from the higher Li^+ diffusion coefficient of 0.006 for the PPFPA-g-Celgard separator (Figure S14a,b, Supporting Information). Furthermore, a smooth transition of ionic concentration can be observed at the nanoscale, the position of 10 in the inset, after Li–ion passing through the PPFPA-g-Celgard separator. On the contrary, the randomly distributed Li^+ flux with the Celgard separator becomes more chaotic (Figure S14c, Supporting Information), which is caused by the "self-enhanced" mechanism located on the Li anode.[45] Hence, PPFPA polymer brushes forming one-dimensionally orientated ion transport channels are favorable for accelerating and homogenizing Li^+ diffusion during Li plating. Besides, the Li deposition behaviors with different grafting densities of PPFPA polymer brushes were also obtained in the simulation (Figure S15, Supporting Information). More compact Li deposition can be observed with the increasing grafting density of PPFPA polymer brushes, which can be facilely achieved by the controllable surface-initiated polymerization process.

As an intuitive demonstration for the dendrite-free Li deposition with PPFPA-g-Celgard separator, ex situ SEM observations were conducted to explore the nucleation and growth behaviors of Li metal facing the PPFPA-g-Celgard separator. As indicated in Figure S16 (Supporting Information), no significant current peaks are observed before voltage reaches 4.4 V versus Li^+/Li, indicating that the PPFPA-g-Celgard separator has excellent electrochemical stability to be compatible with both ether and carbonate electrolytes. In the commercial ether electrolyte system (i.e., 1 M LiTFSI in DOL/DME), the initial Li nuclei based on PPFPA-g-Celgard is much more evenly distributed than the aggregated Li nuclei with the Celgard separator at a rate of 0.5 mA cm^{-2} (Figure 3d). Further increasing the current density to 1 mA cm^{-2}, the Li nuclei starts to grow into dense and smooth Li deposits with the PPFPA-g-Celgard separator, while apparent Li dendrites with loosely packed porous morphology are observed for the cell with the Celgard separator. It has been reported that a carbonate-based electrolyte (i.e., 1 M $LiFP_6$ in EC/DEC) generates a more weak and thinner SEI layer that is easily fractured during unstable Li plating/stripping,[47] but evenly distributed Li nuclei is still observed with the PPFPA-g-Celgard separator in the carbonate-based electrolyte. However, irregular island-like patterns occur in the plated fibrous Li metal with the Celgard separator. Furthermore, more compact and dense Li deposition is achieved for the PPFPA-g-Celgard separator even at 1 mA cm^{-2}, largely outperforming the loose and porous morphology in the Celgard system (Figure S17, Supporting Information). Both simulations and experiments confirm that the rapid ion transport kinetics provided by electronegative PPFPA polymer brushes can redistribute nonuniform Li^+ flux and induce uniform Li deposition, thus effectively maintaining the structural integrity of SEI in both ether and carbonate electrolytes.

Subsequently, the Coulombic efficiency (CE) of cells was conducted to judge the reversibility of Li deposition/dissolution processes. The initial nucleation overpotential was first evaluated in Li | Cu half-cells to display a much lower value of only 19.8 mV for the PPFPA-g-Celgard separator with lithophilic PPFPA polymer chains, compared with the value (50.7 mV) of Celgard (**Figure 4**a). In addition, the cell with the PPFPA-g-Celgard separator holds stable plating/stripping for over 200 cycles with an average CE of 98.4% (Figure 4b), while the CE with the Celgard separator exhibits irregular fluctuations and a sudden drop after 70 cycles due to the repetitive collapse of Li metal and the formation of dead Li at the current density of 0.5 mA cm^{-2}. This phenomenon was further confirmed by the voltage fluctuations in galvanostatic plating/stripping profiles under different cycles (Figure S18, Supporting Information). The cell with the PPFPA-g-Celgard separator also displays an undervoltage hysteresis of 24.2 mV at the 50th cycle, compared with the high overpotential of 68.9 mV for the Clegard separator (Figure 4c). By raising the current density to 1 and 2 mA cm^{-2}, the corresponding nucleation barrier for the PPFPA-g-Celgard separator is still two times lower than that of the Celgard separator (Figure S19, Supporting Information) despite seeing a slight increase to 22.5 and 52.4 mV, respectively. Similarly, the average CE of the PPFPA-g-Celgard

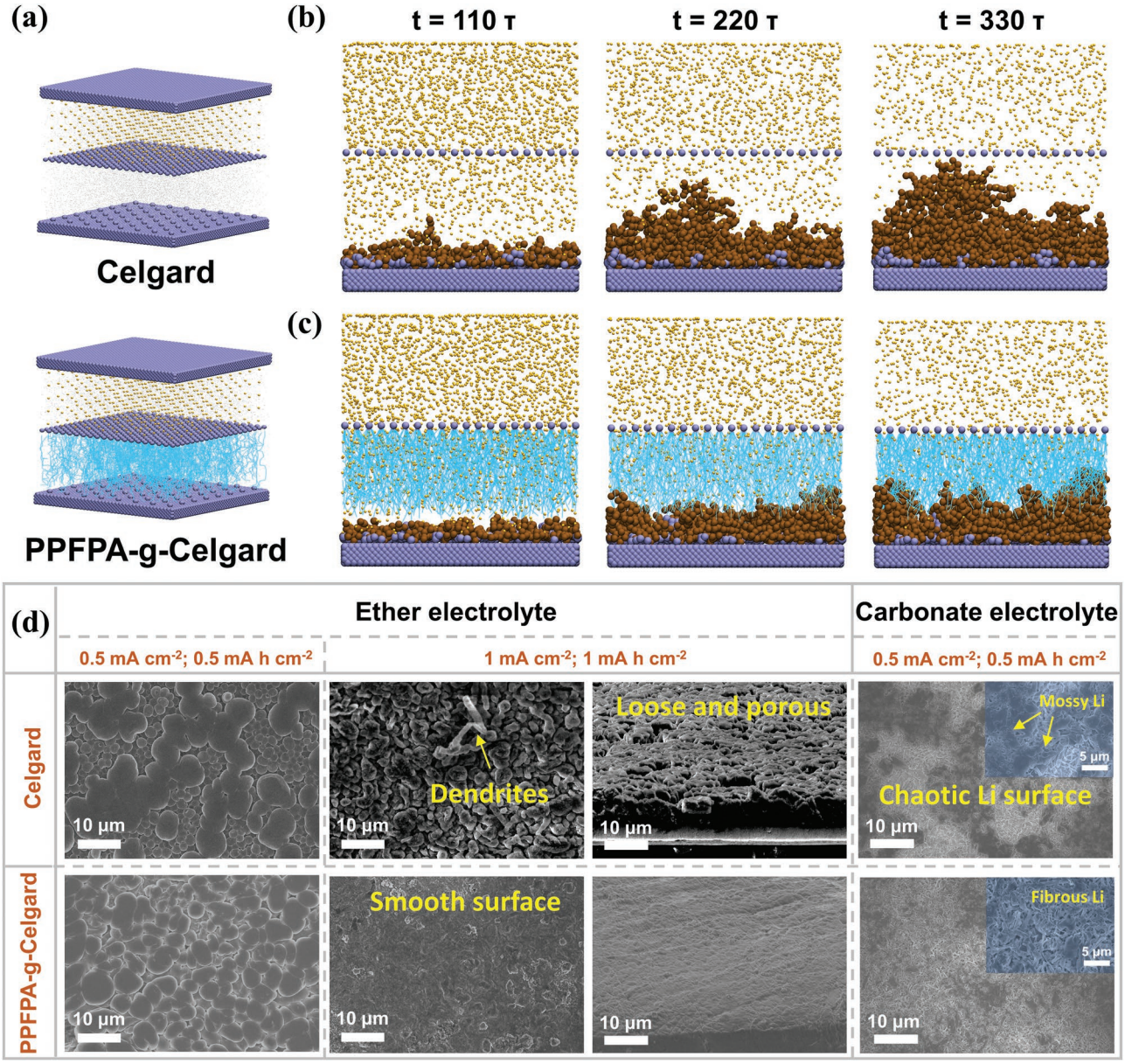

Figure 3. Deposition behaviors of lithium–ions through Celgard and PPFPA-g-Celgard separators using DPD simulation. a) The initial states of the simulation boxes without and with polymer brushes. Deposition behaviors of Li^+ with varied diffusion time: b) without polymer brushes, and c) with polymer brushes. d) SEM images to detect the plating behaviors of Li metal on the Cu substrate using diverse separators and electrolytes.

separator maintains 98.1% and 93.8%, respectively (Figure S20, Supporting Information), which can effectively alleviate the irreversible interfacial side reactions between the Li metal and electrolyte and thus realize a long-life span.

To demonstrate the interfacial stability and cycling reversibility with the PPFPA-g-Celgard separator in long-term plating/stripping processes, the symmetric cells of Li | PPFPA-g-Celgard | Li were performed under different current densities. As shown in Figure 4d, the cells exhibit similar reversible overpotential without obvious oscillation in the beginning. However, obvious voltage polarizations occur for the cell with the Celgard separator in the case of cycling under a given rate of 4 and 6 mA cm^{-2}, accompanied by a threatening short circuit caused by rigid ion transport. By contrast, highly stable voltage hysteresis is obtained with the PPFPA-g-Celgard separator cycling at different current rates in the range of 0.5 to 6 mA cm^{-2} (Figure 4e). Besides, the cell incorporating the PPFPA-g-Celgard separator also delivers a prolonged cycling time of over 900 h (450 cycles) with a flat voltage profile when operating at relatively mild cycling of 1 mA cm^{-2} (Figure 4f). However, the Li | Celgard | Li cell shows a limited life span of only 200 h along with a drastic voltage fluctuation due to the accumulated thick Li passivation layer and cluttered interface resulting from uneven Li^+ transport (Figure S21, Supporting Information). The reduced interfacial resistance in Nyquist plots also suggests a stable interface formed by the electronegative PPFPA polymer chains

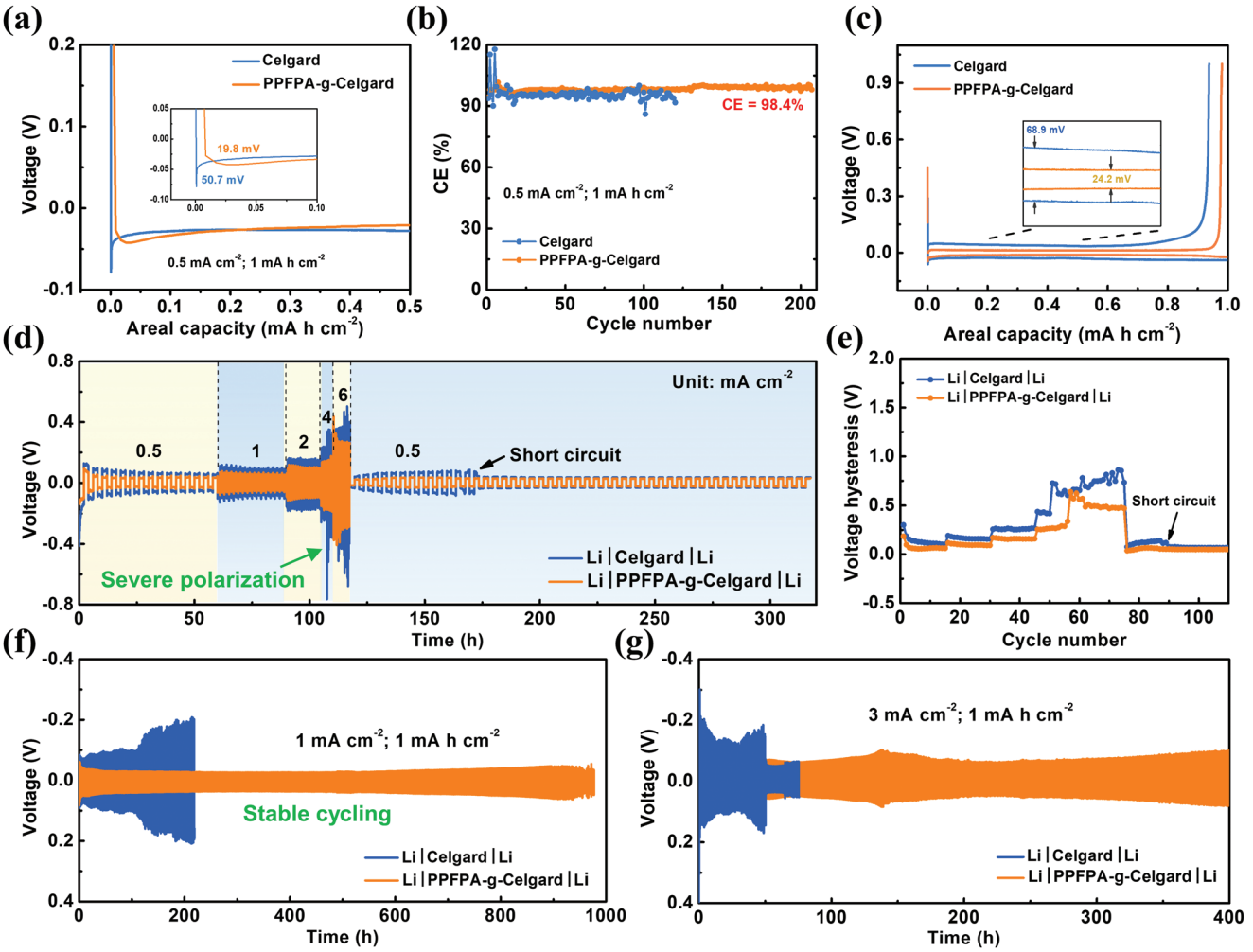

Figure 4. a) Nucleation overpotential, b) CE, and c) the corresponding discharge–charge profiles for a given 50th galvanostatic Li plating/stripping with Celgard and PPFPA-g-Celgard separators at 0.5 mA cm^{-2} with a plating capacity of 1 mA h cm^{-2}. d) Rate performance of different symmetrical cells and e) the corresponding voltage hysteresis. Voltage–time profiles of different separators under different current densities: f) 1 mA cm^{-2}, 1 mA h cm^{-2}; g) 3 mA cm^{-2}, 1 mA h cm^{-2}.

between the separator and electrode, which is beneficial to promoting Li^+ transfer and reducing dendrite growth (Figure S22, Supporting Information). Further raising the current density to 3 and 5 mA cm^{-2}, the PPFPA-g-Celgard separator still maintains steady Li deposition/dissolution for over 400 h (Figure 4g; Figure S23, Supporting Information). Owing to dense Li plating and stable polarization upon long-term cycling, the Li metal anode facing the PPFPA-g-Celgard separator keeps a very flat surface after the 50th cycle (Figure S24a–c, Supporting Information), which is in sharp contrast with a large amount of bulky and mossy Li with obvious dendrites and volume expansion in the cell with the Celgard separator, as evidenced by the SEM images (Figure S24d–f, Supporting Information). Remarkably, the PPFPA-g-Celgard separator also demonstrates excellent long-term effectiveness in the carbonate-based electrolyte (Figure S25, Supporting Information), showing great potential for other energy storage systems.

To satisfy practical demands, the PPFPA-g-Celgard separator was then coupled with the $LiFePO_4$ (LFP) cathode to assemble Li | PPFPA-g-Celgard | LFP full batteries in both ether and carbonate electrolytes (**Figure 5**a). The cyclic voltammetry (CV) curve of the Li | PPFPA-g-Celgard | LFP full battery displays a pair of redox peaks at 3.289 V/3.574 V (vs Li/Li^+), demonstrating normal Li stripping/plating with the PPFPA-g-Celgard separator (Figure S26a, Supporting Information). Meanwhile, the Li | PPFPA-g-Celgard | LFP cell exhibits a smaller curvature diameter than the Li | Celgard | LFP one, indicating a lower charge transfer resistance (R_{ct}) and better ion transfer environment created by the PPFPA-g-Celgard separator (Figure S26b, Supporting Information). As shown in Figure 5b and Figure S27 (Supporting Information), the rate capability differing from 0.1 to 3 C suggests that excellent capacity retention can be achieved by the Li | PPFPA-g-Celgard | LFP full battery. Under a low rate of 0.1 C, a high specific capacity of 150 mA h g^{-1} is obtained for the Li | PPFPA-g-Celgard | LFP full battery. Even when cycling at a high rate of 3 C, it still performs more superior cycling stability with a doubled discharge capacity of 83.9 mA h g^{-1} in comparison with the low capacity

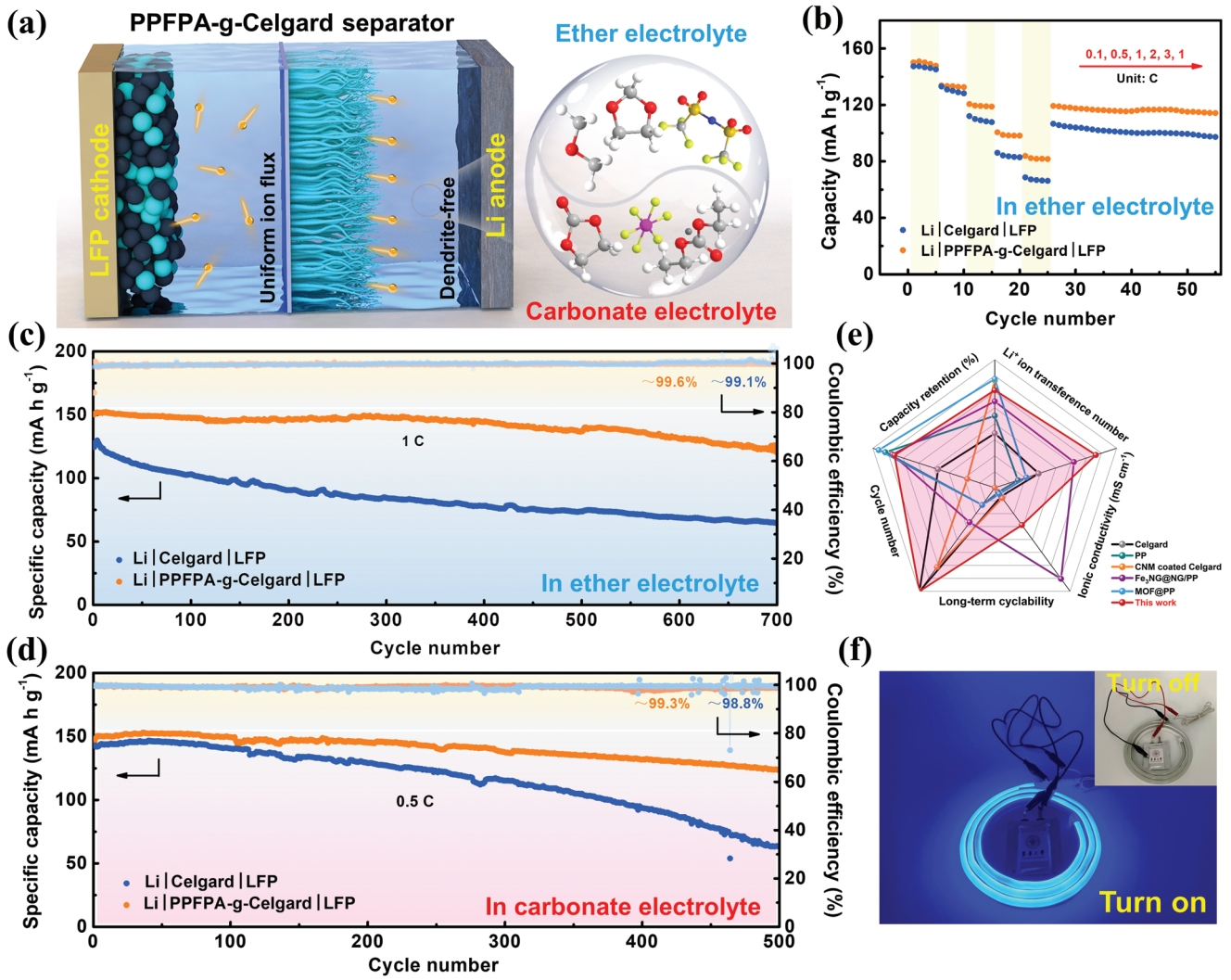

Figure 5. a) Schematic illustration for the construction of Li | PPFPA-g-Celgard | LFP full batteries in different electrolytes. b) Rate capability from 0.1 to 3 C with the ether electrolyte. Long-term cycling performances of Li | PPFPA-g-Celgard | LFP full cell with c) ether electrolyte and d) carbonate electrolyte. e) Radar plots of the PPFPA-g-Celgard separator in comparison with other reported separators modified with physical coatings. f) Digital photographs of the practical Li | PPFPA-g-Celgard | NMC pouch cell lighting up LEDs.

of 45.9 mA h g^{-1} for the Li | Celgard | LFP full battery. When the current density returns to 1 C, the capacity recovers to 119.3 mA h g^{-1}, suggesting the superior capacity stability to the variational rates of the Li | PPFPA-g-Celgard | LFP full battery. Meanwhile, the long-cycling performance of the full batteries with Celgard and PPFPA-g-Celgard separators is obtained at a current density of 1 C (Figure 5c). With an initial discharge capacity of 150.2 mA h g^{-1}, the Li | PPFPA-g-Celgard | LFP full battery offers relatively stable long cycling with a CE of 99.6% and capacity retention of 83% for >700 cycles. However, the full battery with the bare Celgard separator only exhibits a relatively low initial capacity of 124.6 mA h g^{-1}, with a fast-faded discharge capacity of 64.6 mA h g^{-1} after 700 cycles. Besides, the Li | PPFPA-g-Celgard | LFP full battery also shows greatly enhanced long-cycle performance in the carbonate-based electrolyte with a capacity retention of 85.4% for over 500 cycles (Figure 5d). The PPFPA-g-Celgard separator delivers a significant advance in cycling performance among the previously reported separators for the practical application of LMBs (Figure 5e; Tables S3 and S4, Supporting Information). To further clarify the reasons behind capacity contribution, multiple CV tests at different scan rates were performed to analyze the Li–ion diffusion coefficient (Figure S28, Supporting Information). Clearly, the PPFPA-g-Celgard separator shows large slope and faster ion diffusion than Celgard, being consistent with the results of enhanced ionic conductivity and ion transference number (Figure 2i). The advantages of using the PPFPA-g-Celgard separator for enhanced electrochemical kinetics are then directly reflected in greatly enhanced capacity and rate-capability behaviors. Additionally, the PPFPA-g-Celgard separator derived SEI layer in Figure S29 (Supporting Information) is favorable for stable Li plating and striping. An apparent C—F bond was detected on the surface of the PPFPA-g-Celgard separator even undergoing long-term cycling, indicating the very

stable chemical topology structure of PPFPA polymer chains (Figure S30, Supporting Information). To better present the universal advantage of the topochemically modified separator, it was also coupled with the $LiNi_{0.8}Co_{0.1}Mn_{0.1}O_2$ (NMC) cathode to fabricate the Li | PPFPA-g-Celgard | NMC pouch cell for practical validation. As illustrated in Figure 5f, the thin pouch cell has a size of 3 cm × 6 cm, which can successfully light up light-emitting-diode (LED) lamps with a voltage of 5 V. This further proves that the electronegative polymer brush-grafted separator possesses excellent chemical stability to stabilize the Li metal anode and has great potentials for replication and large-scale applications.

3. Conclusion

Guided by the strong electronegativity of F and O atoms, a novel separator modification strategy of stabilizing the Li metal anode was proposed by the PDA-assistant SI-ATRP grafting of electronegative PPFPA polymer brushes on the surface of the conventional polyolefin separator. One-dimensionally aligned polymer brushes can precisely control directed and rapid ion transport at the nanoscale through the lithiophilicity paths in PPFPA chains. Hence, the high Li transference number of 0.61 and increased ionic conductivity of 8.33×10^{-4} S cm^{-1} is achieved for the PPFPA-g-Celgard separator, which almost outperform those of the Clegard separator by two times. Due to well-matched synergistic effects, the PPFPA-g-Celgard separator can be compatible with both carbonate and ether-based electrolytes. Therefore, smooth Li deposition can be achieved in half-cells along with very long-term stripping/platting without dendrite growth. The proof-of-concept demonstration in the molecular level engineering of conventional separators to endow uniform ion flux and dendrite-free Li deposition would provide pilot reference and extend potential applications for other advanced energy-storage systems.

Supporting Information

Supporting Information is available from the Wiley Online Library or from the author.

Acknowledgements

This work was financially supported by the National Natural Science Foundation of China (22075042, 51925207, U1910210, 52161145101 and 51872277), Natural Science Foundation of Shanghai (20ZR1401400), the Strategic Priority Research Program of Chinese Academy of Sciences (Grant No. XDA21000000), the National Synchrotron Radiation Laboratory (KY2060000173), the Joint Fund of the Yulin University and the Dalian National Laboratory for Clean Energy (Grant. YLU-DNL Fund 2021002) and the Fundamental Research Funds for the Central Universities and DHU Distinguished Young Professor Program (LZB2021002).

Conflict of Interest

The authors declare no conflict of interest.

Data Availability Statement

Research data are not shared.

Keywords

electrodepositions, functional separators, homogenized ion flux, polymer brushes, topochemical polymerizations

Received: February 4, 2022
Revised: June 30, 2022
Published online: August 4, 2022

[1] F. Wu, J. Maier, Y. Yu, *Chem. Soc. Rev.* **2020**, *49*, 1569.
[2] G. Li, *Adv. Energy Mater.* **2021**, *11*, 2002891.
[3] X. Chen, B. Zhao, C. Yan, Q. Zhang, *Adv. Mater.* **2021**, *33*, 2004128.
[4] C. Zhou, W. Zong, G. Zhou, X. Fan, Y. Miao, *Compos. Commun.* **2021**, *25*, 100696.
[5] Y. Liu, Y. Zhai, Y. Xia, W. Li, D. Zhao, *Small Struct* **2021**, *2*, 2000118.
[6] W. Liu, Z. Chen, Z. Zhang, P. Jiang, Y. Chen, E. Paek, Y. Wang, D. Mitlin, *Energy Environ. Sci.* **2021**, *14*, 382.
[7] X. Yue, Q. Zhou, J. Bao, C. Ma, S. Yang, X. Li, D. Sun, F. Fang, X. Wu, Y. Zhou, *Adv. Funct. Mater.* **2021**, *31*, 2008786.
[8] C. Zhao, X. Yao, H. Yang, X. Jiao, L. Wang, *Compos. Commun.* **2021**, *26*, 100789.
[9] Y. Zhong, S. Zhou, Q. He, A. Pan, *Energy Storage Mater.* **2022**, *45*, 48.
[10] C. Yan, P. Zhu, H. Jia, J. Zhu, R. K. Selvan, Y. Li, X. Dong, Z. Du, I. Angunawela, N. Wu, M. Dirican, X. Zhang, *Adv. Fiber Mater.* **2019**, *1*, 46.
[11] P. Bai, J. Li, F. R. Brushett, M. Z. Bazant, *Energy Environ. Sci.* **2016**, *9*, 3221.
[12] W. Xu, C. Tang, N. Huang, A. Du, M. Wu, J. Zhang, H. Zhang, *S. Sci.* **2022**, *2*, 2100105.
[13] Y. Jie, X. Ren, R. Cao, W. Cai, S. Jiao, *Adv. Funct. Mater.* **2020**, *30*, 1910777.
[14] D. Aurbach, E. Markevich, G. Salitra, *J. Am. Chem. Soc.* **2021**, *143*, 21161.
[15] Q. Yang, J. Hu, J. Meng, C. Li, *Energy Environ. Sci.* **2021**, *14*, 3621.
[16] Y. Wang, Z. Wang, L. Zhao, Q. Fan, X. Zeng, S. Liu, W. K. Pang, Y. He, Z. Guo, *Adv. Mater.* **2021**, *33*, 2008133.
[17] Y. Chen, G. Zhou, W. Zong, Y. Ouyang, K. Chen, Y. Lv, Y. Miao, T. Liu, *Compos. Commun.* **2021**, *25*, 100679.
[18] W. Cai, C. Yan, Y. Yao, L. Xu, R. Xu, L. Jiang, J. Huang, Q. Zhang, *Small Struct* **2020**, *1*, 2000010.
[19] C. Jin, J. Nai, O. Sheng, H. Yuan, W. Zhang, X. Tao, X. Lou, *Energy Environ. Sci.* **2021**, *14*, 1326.
[20] X. Chen, X. Chen, T. Hou, B. Li, X. Cheng, R. Zhang, Q. Zhang, *Sci. Adv.* **2019**, *5*, eaau7728.
[21] M. Qi, Y. Xu, S. Guo, S. Zhang, J. Li, Y. Sun, K. Jiang, A. Cao, L. Wan, *Small Sci.* **2021**, *1*, 2100066.
[22] G. Jiang, F. Li, H. Wang, M. Wu, S. Qi, X. Liu, S. Yang, J. Ma, *Small Struct* **2021**, *2*, 2000122.
[23] X. Cheng, R. Zhang, C. Zhao, Q. Zhang, *Chem. Rev.* **2017**, *117*, 10403.
[24] Y. Zhou, X. Zhang, Y. Ding, J. Bae, X. Guo, Y. Zhao, G. Yu, *Adv. Mater.* **2020**, *32*, 2003920.
[25] X. Li, M. Lv, Y. Tian, L. Gao, T. Liu, Q. Zhou, Y. Xu, L. Shen, W. Shi, X. Li, Y. Lu, X. Liu, S. Xiao, *Nano Energy* **2021**, 106214.

[26] A. Hu, W. Chen, X. Du, Y. Hu, T. Lei, H. Wang, L. Xue, Y. Li, H. Sun, Y. Yan, J. Long, C. Shu, J. Zhu, B. Li, X. Wang, J. Xiong, *Energy Environ. Sci.* **2021**, *14*, 4115.
[27] X. Meng, Y. Sun, M. Yu, Z. Wang, J. Qiu, *Small Sci* **2021**, *1*, 2100021.
[28] S. Chang, X. Jin, Q. He, T. Liu, J. Fang, Z. Shen, Z. Li, S. Zhang, M. Dahbi, J. Alami, K. Amine, A. Li, H. Zhang, J. Lu, *Nano Lett.* **2022**, *2*, 263.
[29] Z. Li, M. Peng, X. Zhou, K. Shin, S. Tunmee, X. Zhang, C. Xie, H. Saitoh, Y. Zheng, Z. Zhou, Y. Tang, *Adv. Mater.* **2021**, *33*, 2100793.
[30] M. Zhang, H. Wang, B. Peng, D. Ma, M. Bai, X. Tang, S. Li, W. Zhao, S. Liu, Z. Wang, K. Zhou, C. Sun, Y. Ma, *Cell Rep. Phys. Sci.* **2021**, *2*, 100324.
[31] N. Li, Q. Ye, K. Zhang, H. Yan, C. Shen, B. Wei, K. Xie, *Angew. Chem., Int. Ed.* **2019**, *131*, 18414.
[32] C. Jiao, C. Zhao, Y. Ma, W. Yang, *ACS Nano* **2021**, *15*, 15920.
[33] G. Gao, Y. Wang, S. Wang, R. Yang, Y. Chen, Y. Zhang, C. Jiang, M. Wei, H. Ma, Y. Lan, *Angew. Chem., Int. Ed.* **2021**, *60*, 10147.
[34] Z. Hao, Y. Wu, Q. Zhao, J. Tang, Q. Zhang, X. Ke, J. Liu, Y. Jin, H. Wang, *Adv. Funct. Mater.* **2021**, 2102938.
[35] Z. Hao, Q. Zhao, J. Tang, Q. Zhang, J. Liu, Y. Jin, H. Wang, *Mater. Horiz.* **2021**, *8*, 12.
[36] C. Zhang, L. Xiang, J. Zhang, C. Liu, Z. Wang, H. Zeng, Z. K. Xu, *Chem. Sci.* **2022**, *13*, 1698.
[37] S. Rajendran, Z. Tang, A. George, A. Cannon, C. Neumann, A. Sawas, E. Ryan, A. Turchanin, L. M. R. Arava, *Adv. Energy Mater.* **2021**, *11*, 2100666.
[38] D. Zhou, X. Tang, X. Guo, P. Li, D. Shanmukaraj, H. Liu, X. Gao, Y. Wang, T. Rojo, M. Armand, G. Wang, *Angew. Chem., Int. Ed.* **2020**, *132*, 16868.
[39] B. D. Ippel, M. I. Komil, P. A. A. Bartels, S. H. M. Söntjens, R. J. E. A. Boonen, M. M. J. Smulders, P. Y. W. Dankers, *Macromolecules* **2020**, *53*, 4454.
[40] S. Wang, H. Meng, Y. Li, D. Sun, Y. Zhan, X. Ge, L. Chen, *J. Polym. Sci. Part Polym. Chem.* **2019**, *57*, 689.
[41] D. Hafner, R. Jordan, *Polym. Chem.* **2020**, *11*, 2129.
[42] M. Zhou, R. Liu, D. Jia, Y. Cui, Q. Liu, S. Liu, D. Wu, *Adv. Mater.* **2021**, *33*, 2100943.
[43] Y. Que, J. Ruan, Y. Xiao, C. Feng, G. Lu, X. Huang, *Polym. Chem.* **2020**, *11*, 1727.
[44] Q. Lu, X. Zou, R. Ran, W. Zhou, K. Liao, Z. Shao, *J. Mater. Chem. A* **2019**, *7*, 22463.
[45] J. Xiao, *Science* **2019**, *366*, 426.
[46] Q. Zhang, P. Chen, C. Yan, P. Chen, R. Zhang, Y. Yao, H. Peng, L. Yan, S. Kaskel, *Angew. Chem., Int. Ed.* **2021**, *60*, 18031.
[47] P. Liu, H. Hao, H. Celio, J. Cui, M. Ren, Y. Wang, H. Dong, A. R. Chowdhury, T. Hutter, F. A. Perras, J. Nanda, J. Watt, D. Mitlin, *Adv. Mater.* **2021**, *34*, 2105855.